Hindawi Publishing Corporation
Journal of Nanomaterials
Volume 2014, Article ID 471485, 14 pages
http://dx.doi.org/10.1155/2014/471485

Review Article

Fabrication, Characterization, Properties, and Applications of Low-Dimensional $BiFeO_3$ Nanostructures

Heng Wu, Jun Zhou, Lizhi Liang, Lei Li, and Xinhua Zhu

National Laboratory of Solid State Microstructures, School of Physics, Nanjing University, Nanjing 210093, China

Correspondence should be addressed to Xinhua Zhu; xhzhu1967@aliyun.com

Received 25 April 2014; Revised 25 June 2014; Accepted 25 June 2014; Published 25 August 2014

Academic Editor: Seungbum Hong

Low-dimensional $BiFeO_3$ nanostructures (e.g., nanocrystals, nanowires, nanotubes, and nanoislands) have received considerable attention due to their novel size-dependent properties and outstanding multiferroic properties at room temperature. In recent years, much progress has been made both in fabrications and (microstructural, electrical, and magnetic) in characterizations of $BiFeO_3$ low-dimensional nanostructures. An overview of the state of art in $BiFeO_3$ low-dimensional nanostructures is presented. First, we review the fabrications of high-quality $BiFeO_3$ low-dimensional nanostructures *via* a variety of techniques, and then the structural characterizations and physical properties of the $BiFeO_3$ low-dimensional nanostructures are summarized. Their potential applications in the next-generation magnetoelectric random access memories and photovoltaic devices are also discussed. Finally, we conclude this review by providing our perspectives to the future researches of $BiFeO_3$ low-dimensional nanostructures and some key problems are also outlined.

1. Introduction

Multiferroics are formally defined as materials that exhibit more than one primary ferroic order parameter simultaneously [1, 2]. The coupling of different order parameters such as magnetoelectric coupling reveals the mutual regulation of magnetic and electric field which has potentially enormous commercial value in the next generation of information technology areas (e.g., multistate storage) [3–7]. Among the single-phase multiferroics, $BiFeO_3$ (BFO) has high Curie temperature (T_C = 850°C), high Neel temperature (T_N = 370°C), and large residual polarization intensity (150 μC/cm^2) at room temperature, which is widely investigated as model system of single-phase multiferroics. However, as one kind of G-type antiferromagnetic material BFO has spiral spin structure with a periodicity of 62 nm, this weak liner magnetoelectirc coupling makes it hard to be used in multifunctional devices [8]. Recently, it is found that the BFO nanoparticles exhibit relatively strong ferromagnetism as their sizes are below 62 nm [9]. Therefore, an enhanced magnetoelectric coupling can be achieved in the nanosized BFO materials, which play an important role in microelectronic devices [10–12]. Recent advances in science and technology of semiconductor integrated circuit have resulted in the feature sizes of microelectronic devices downscaling into nanoscale dimensions. At nanoscale the BFO materials display novel physical properties that are different from their bulk and film counterparts. Understanding the size effects of the BFO materials at nanoscale is of importance for developing the next generation of revolutionary electronic nanodevices. Due to the size effects being dependent on the structure and finite size, considerable efforts have been made in the controllable synthesis of low-dimensional BFO nanostructures such as nanowires, nanotubes, and their arrays. Much progress has also been achieved in the structure and property characterization. Furthermore, BFO nanostructures are also received extensive attention in the study of heterostructures [13] and domain characterizations [14–16]. This paper provides an overview of recent advances on the fabrication, structural characterization, and physical properties of low-dimensional BFO nanosized materials. Their potential applications are also discussed and some problems that need to be solved in future researches are also pointed out.

2. Fabrication of Low-Dimensional BFO Nanostructures

Generally, nanostructured materials can be classified into four classes by their dimensions, which are zero-dimensioned (0D) structures such as nanoparticles, one-dimensioned (1D) materials such as nanowires, nanorods, and nanotubes, two-dimensioned (2D) materials such as thin film and nanoislands, and three-dimensioned (3D) materials such as nanowires/tubes arrays, respectively. Up to date, two different approaches have been developed to fabricate nanostructured BFO, one is the bottom-up approach which means synthesizing nanostructures from atoms or molecules by assembling tiny into large, the other one is top-down approach which means dividing, etching or carving thin film or bulk materials into nanostructures as cutting big into small. In this section, we introduce the most used techniques for fabrication of low-dimensional BFO nanostructures and discuss their differences.

2.1. Sol-Gel Process. Sol-gel process is a kind of bottom-up approach, which generally involves the use of metal alkoxides and undergoes hydrolysis and condensation polymerization reactions to produce gels. After annealing the gels transform the porous gels into a dense target product. The main processing factors of sol-gel process are the water ratio in solution, pH value of solution, and its temperature. To synthesize BFO nanoparticles by sol-gel process, $Bi(NO_3)_3 \cdot 5H_2O$ and $Fe(NO_3)_3 \cdot 9H_2O$ are normally used as the raw materials. For example, Kim et al. [17] synthesized the BFO powders (average sizes ~200 nm) by dissolving $Bi(NO_3)_3 \cdot 5H_2O$ into the mixture of 2-methoxyethanol and acetic acid, and as the solution became transparent they dissolved $Fe(NO_3)_3 \cdot 9H_2O$ in it and kept the mixture at room temperature with stirring. Then, the precursor solution was dried at 80°C for about 12 h to obtain the BFO xerogel powder. They grinded the xerogel powders and annealed them at 600°C in air or N_2 atmosphere to obtain the BFO nanosized powders. Gao et al. [18] dissolved the $Bi(NO_3)_3 \cdot 5H_2O$ and $Fe(NO_3)_3 \cdot 9H_2O$ with stoichiometric proportions into 2-methoxyethanol and adjusted the solution pH value to 4-5 by adding nitric acid subsequently. Then citric acid in 1 : 1 molar ratio with the metal nitrates and polyethylene glycol as a dispersant was added into the solution, respectively. After stirring the solution at 50°C for 0.5 h, the solution was kept at 80°C for 4 days to obtain the dried gel. After calcination at 500°C for 2 h perovskite-type BFO nanoparticles with average diameter of ~80–120 nm were obtained. Similarly, Park et al. [9] also employed the sol-gel process to synthesize single-crystalline BFO nanoparticles and tuned their sizes from less than 15 nm to ~100 nm by changing the annealing temperatures. Obviously, the sizes of BFO nanoparticle were increased with the annealing temperature. However, the ideal synthetic pathway for the BFO nanoparticles is to obtain the appropriate size, shape, and crystallinity in the absence of the additional postannealing steps. Therefore, modified sol-gel techniques are developed to synthesize the BFO nanoparticles. Among them, hydrothermal method is one of the examples, in which there is no necessity for high-temperature calcination.

2.2. Hydrothermal Method. Hydrothermal method is also called the autoclave method, which involves heating an aqueous suspension of insoluble salts in an autoclave at a moderate temperature and pressure so that the crystallization of a desired phase will take place. The hydrothermal method is very popular method for synthesizing the perovskite nanoparticles because the synergetic effects from solvent, temperature, and pressure can offer stable final products and prevent the formation of impurity phases. The hydrothermal method is used to synthesize the BFO nanoparticles. For example, Chen et al. [19] utilized $Bi(NO_3)_3 \cdot 5H_2O$ and $Fe(NO_3)_3 \cdot 9H_2O$ as raw materials and adjusted the concentration of KOH at the region 1 M to 9 M to synthesize BFO nanoparticles with different morphologies at 200°C for 6 h. Han et al. [20] used $Bi(NO_3)_3 \cdot 5H_2O$, $Fe(NO_3)_3 \cdot 9H_2O$ and 8 M KOH to synthesize pure BFO powders at the temperatures of 175–225°C and the hold time of 6 h, respectively. Wang et al. [21] used $Bi(NO_3)_3 \cdot 5H_2O$ and $Fe(NO_3)_3 \cdot 9H_2O$ as raw materials and synthesized the different morphologies of BFO nanoparticles by adding KNO_3 mineralizer or not. All the above results demonstrate that the concentration of KOH determines the phase structure of the synthesized products. The pure BFO nanoparticles with diameters of 100–300 nm were synthesized when the concentration of KOH was 7 M and 12 M. If the concentration of KOH was below, the synthesized products were mainly composed of perovskite-type BFO accompanied with impurity phase of orthorhombic-type $Bi_2Fe_4O_9$. In hydrothermal procedure, the growth rate of $BiFeO_3$ was decreased by adding the KNO_3 mineralizer, and thin plate-like $BiFeO_3$ could be obtained as increasing the reaction time.

In addition, the solvothermal method is also a popular method to synthesize the BFO nanomaterials, which is similar to the hydrothermal method. The only difference is that the precursor solution for a solvothermal method is usually an organic medium such as ethanol or acetone, while that for a hydrothermal method is usually an aqueous medium such as water. Liu et al. [22] employed solvothermal method to synthesize single-crystalline BFO nanowires (45–200 nm in diameter, several nanometers to several micrometers in length) in acetone solvent. They dissolved $Bi(NO_3)_3 \cdot 5H_2O$ and $Fe(NO_3)_3 \cdot 9H_2O$ in 1 : 1 molar ratio then added deionized water and stronger ammonia water to adjust pH value of the solution to 10-11. After washing the sediment by distilled water until it is neutral, 5 M NaOH was added and kept stirring for 30 min. Then they heated the solution at 180°C for 72 h hand obtained the single-crystalline BFO nanowires.

Moreover, the morphology of the final products derived from solvothermal method can be effectively controlled by selecting the types of organics and their amount. For example, Zhang et al. [23] synthesized BFO nanoparticles and nanowires assembled by nanoparticles via changing the amount of the PVP or PEG (polyethylene glycol) polymer.

2.3. Template Method. Template method is based on chemical self-organization to synthesize nanostructured materials by the assistance of template which is porous with nanosized pores. By electrochemical deposition, sol-gel or chemical vapor deposition technology, atoms, or ions are deposited on

Table 1: Summary of various approaches for fabricating the BFO low-dimensional nanostructures.

Approaches	Advantages	Disadvantages	Structures
Bottom-up			
Sol-gel	Facile regulation Low reaction temperature	Long reaction time	Nanoparticle
Template	Easy process uniform size and array	Limited aspect ratio	Nanowire/tube
Hydrothermal	Easy process high crystallinity low reaction temperature	Harsh reaction condition	Nanoparticle/wire
Top-down			
FIB	High resolution uniform size and array	Surface damage low throughput	Nanoisland/array

the tube walls and form the nanostructure. Template method can be employed to fabricate one-dimensioned materials which have well dispersion and are easy to adjust aspect ratio of nanowires, tubes, and rods by changing the structural parameters of the used templates. Since the nanostructures fabricated by template method have similar structural properties (e.g., sizes, shape) to the templates, therefore, the pore sizes and their aspect ratios of the templates are crucial parameters for controlling the dimensions of the final nanostructures. Park et al. [24] first reported on the synthesis of BFO nanotubes by using porous anodic alumina (AAO) templates with pore-size of 100 or 200 nm. They dissolved $Bi(NO_3)_3 \cdot 5H_2O$ and $Fe(NO_3)_3 \cdot 9H_2O$ with a molar ratio of 1:1 to ethylene glycol and deposited the sol onto the surface of the AAO template by using a syringe. Finally they obtained BFO nanotubes with outer diameters in the range of 240 to 300 nm (for 200 nm pore-sized template) or 140 to 180 nm (for 100 nm pore-sized template) and lengths ranging from several microns to as much as 50 μm. However, the synthesized BFO nanotubes are polycrystalline because of the random nucleation on the walls of pores. Zhang et al. [25] also employed the similar method to synthesize BFO nanowires array *via* injecting the sol on the template and annealed it subsequently. Gao et al. [26] synthesized polycrystalline BFO nanowires with a diameter of 50 nm and 5 μm in length by the similar method.

Synthesis of the BFO nanostructures by template method provides some advantages such as the structure of the nanoarray subject to the structure of the template, the channels of the template controlling the dimension of the materials, template pore walls preventing the aggregation of the material, and a large amount of nanowires or nanotubes mass produced.

2.4. Focus Ion Beam (FIB) Milling Method. The common top-down approach to fabricate nanostructured materials is focused ion beam (FIB) milling method. The typical technology is to utilize focused Ga^+ ions to bombard the thin film or bulk material to obtain the designed nanostructures. The advantages of FIB milling method are controllable morphology of structure or even patterns, facile operation and, and so forth. However, the disadvantages are high cost and the resolution of FIB is micron or submicron scale which is larger than the nanostructure.

Recently, Morelli et al. [27] fabricated BFO nanoislands by template-assisted FIB method based on epitaxial BFO thin films grown on $SrTiO_3$ (100) substrates. Arrays of 45 nm-thick aluminium dots were first evaporated on BFO thin films through template with aperture diameter of 400 nm. A focused ion beam with gallium ions was used to mill the specimen covered by Al dots. Chemical etching of the remaining Al was performed in 10% aqueous solution of potassium hydroxide (KOH) at room temperature for 90 s. Arrays of epitaxial BFO nanoislands with diameter ~250 nm were obtained. The features of top-down approaches are their precisely positioning and controlling the shapes and sizes of the designed BFO nanostructures. However, their time-consuming and low-throughput characters of these processes are the shortcomings of the top-down approaches.

Table 1 summarizes various approaches for fabricating the BFO low-dimensional nanostructures.

3. Characterization of BFO Nanostructures

Up to date various approaches including X-ray diffraction (XRD), scanning electron microscopy (SEM), (high-resolution) scanning transmission electron microscopy (HR) STEM, as well as X-ray energy dispersive spectrum (EDS), electron energy loss spectra (EELS), and selected area electron diffraction (SAED) have been developed to probe both the macroscopic and the microscopic details of BFO low-dimensional nanostructures. In this section, we will briefly summarize the recent the atomic-scale microstructural features of BFO low-dimensional nanostructures revealed a number of techniques.

3.1. BFO Nanoparticles/Nanoislands. Park et al. [9] first reported the synthesis of pure crystalline BFO nanoparticles by sol-gel method. Figure 1 shows the structural characterizations of BFO nanoparticles with the average diameter of 95 nm by techniques of TEM, SAED, EDS, and HRTEM. Zhu et al. [28] also reported on the microwave-hydrothermal synthesis of spherical BFO nanoparticles, their TEM and

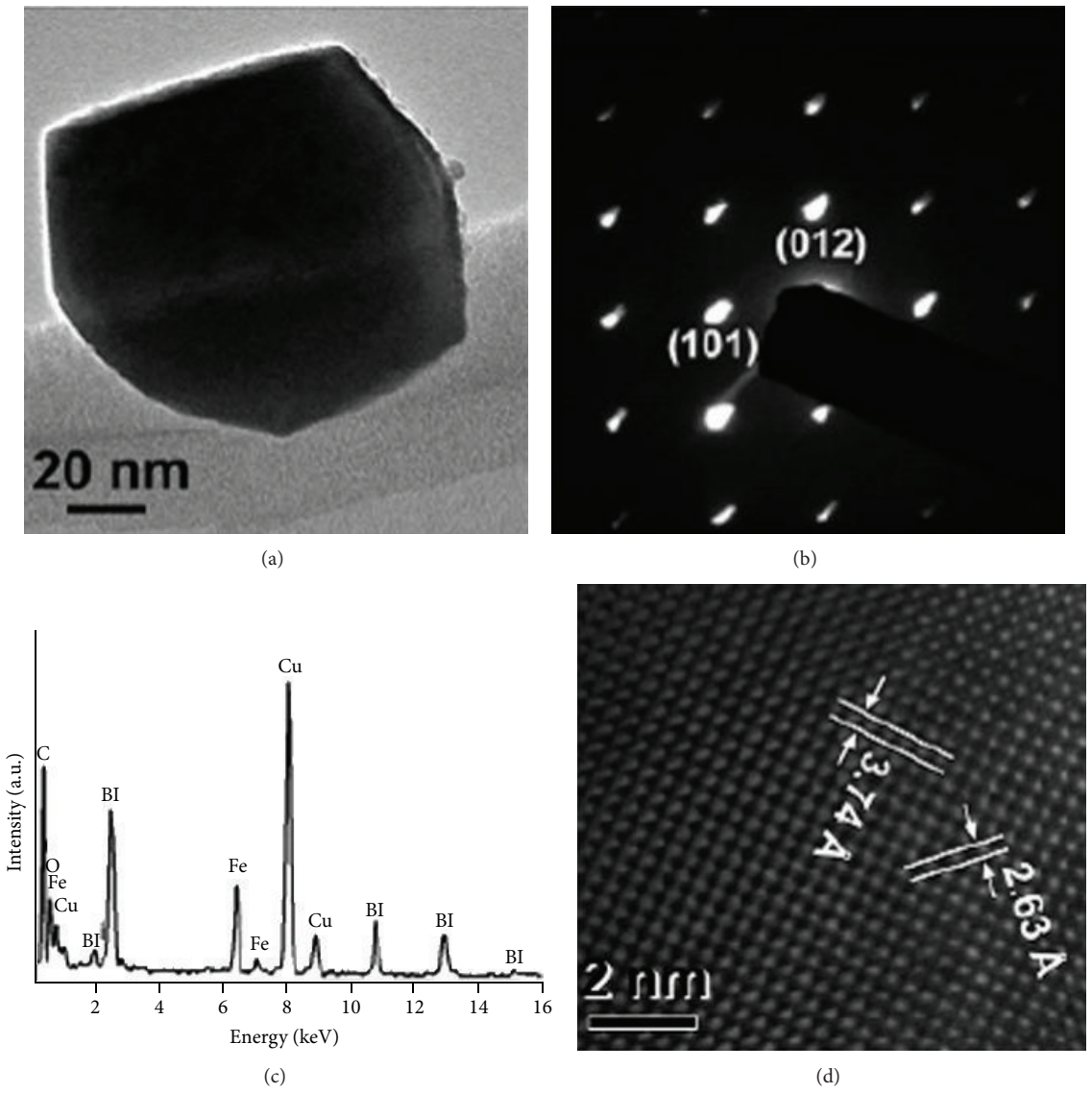

Figure 1: (a) TEM image, (b) SAED pattern, (c) EDS, and (d) HRTEM image of an individual $BiFeO_3$ nanoparticle (with a diameter of 95 nm) synthesized by sol-gel method.

HRTEM images are shown in Figure 2. The HRTEM pattern demonstrates the well crystallization of as-prepared BFO nanocrystals.

Besides the BFO nanoparticles, epitaxial BFO nanoislands were also synthesized by chemical self-assembled method [29], their phase structure and morphology were characterized by XRD and atomic force microscopy (AFM). Figure 3 shows the XRD patterns of the BFO nanoislands annealed at different temperatures; there is almost no other impurity peaks except the diffraction peaks of single crystalline $SrTiO_3$ substrate and the (100) crystal orientation of BFO. The AFM images shown in Figure 4 revealed that with increasing the postannealing temperature from 600°C to 800°C, the morphology of BFO nanoislands in the (100) growth plane evolved from triangled to squared, and then to plated shapes. Fractal ferroelectric domains and self-bias polarization were also found in a single BFO nanoisland, which were revealed by piezoforce microscopy (PFM) images.

Zhou et al. [30] also fabricated the BFO nanoring structure by combing sol-gel, AAO template-assisted, and planar TEM sample preparation methodology. Figure 5(a) shows the STEM image of the nanorings, where the atoms with high atomic numbers (such as Bi, Fe) exhibit bright image contrast; therefore, the BFO nanorings demonstrate high white bright contrast. Figure 5(b) shows the line scan of the intensity distribution of the STEM image contrast of the BFO nanorings, from which the inner diameter of the nanoring was determined to be about 170 nm and its thickness was about 20 nm. Therefore, the BFO nanorings were formed in the walls of the AAO template. The EDS data reveal that the BFO nanorings are composed of Bi, Fe, and O elements and that the chemical composition of the nanorings is close to $BiFeO_3$.

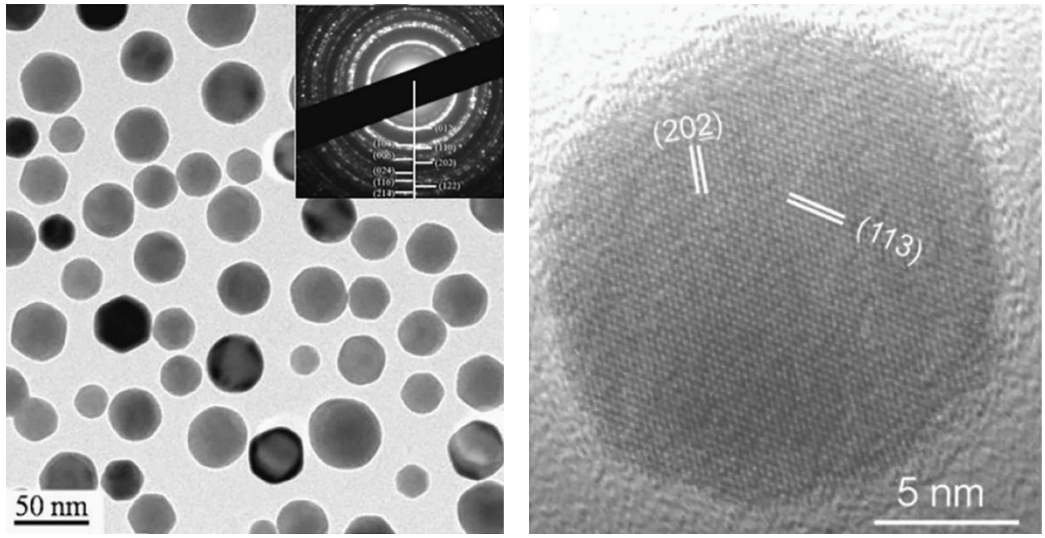

(a) (b)

Figure 2: (a) TEM image of $BiFeO_3$ nanocrystals and the inset is selected area electron diffraction pattern, (b) HRTEM image of a single $BiFeO_3$ nanocrystal with a diameter of ~12 nm.

3.2. One-Dimensional BFO Nanostructures and Their Arrays. Zhang et al. [25, 31] fabricated the BFO nanowire and nanotube arrays by a template synthesis involving the sol-gel technique. Figure 6 shows the SEM images of the BFO nanowire and nanotube arrays, respectively. The TEM image of a single BFO nanotube is shown in Figure 6(c); the corresponding SAED pattern and the EDX spectrum are shown as insets.

3.3. Domain Structures of BFO Thin Films. Chu et al. [32] characterized the ferroelectric polarization direction and domain structures of BFO films with different thicknesses (120, 15, and 2 nm) grown on $SrTiO_3$ (001) (top) and $DySrO_3$ (110) substrates (bottom) by PFM. Due to the competition between the normal strain caused by lattice mismatch and shear strain caused by the rhombohedral symmetry, ferroelectric polarization direction and domain structures are changed with the decrease of the film thickness, as shown in Figure 7. With decreasing the thickness of BFO films deposited on $SrTiO_3$ (001), the domain morphology evolved from stripe domain structures (Figure 7(a)) to intricate domain structures with fluctuate mottled contrast (Figures 7(b) and 7(c)). However, the domain size became larger as decreasing the thickness of BFO films deposited on $DySrO_3$ (110) substrates. Such a difference arises from the normal strain since it cannot be released at such thicknesses; therefore, BFO films on $SrTiO_3$ have larger elastic strain energy, which leads to smaller domain structures.

4. Physical Properties of Low-Dimensional BFO Nanostructures

4.1. BFO Nanoparticles. Park et al. [9] synthesized the BFO nanoparticles by sol-gel method and investigated the size-driven magnetism of the BFO nanoparticles, as shown in Figure 8. As the sizes of the BFO nanoparticles were reduced, their magnetism was significantly enhanced. Especially, when the particle size was 14 nm, the magnetization was about 3 times larger than that of the BFO particle with size of 100 nm. This is important for enhancing the magnetic properties of the BFO nanoparticles with antiferromagnetic ground state.

Recently it is reported that low-dimensional nanostructured BFO such as nanoparticles and nanowires exhibit good photocatalytic activities in visible-light region. As a novel visible-light-responsive photocatalysts for degradation of organic compounds BFO nanostructures have been widely investigated. For example, Zhu et al. [28] reported the microwave-hydrothermal synthesis of spherical perovskite-type BFO nanocrystals with diameters of 10–50 nm and hexagonal-shaped sillenite-type ones with sizes of 18–33 nm at low temperatures. They found that the sillenite-type bismuth ferritic nanocrystals exhibit higher photocatalytic ability than the perovskite-type ones, which was ascribed to their small mean particle sizes and the unique hexagonal-shape morphology, and also the structural characteristics of sillenite-type compound. Gao et al. [18] also reported visible-light photocatalytic property of BFO nanocrystals. As compared with the traditional TiO_2-based photocatalysts, which are the only response to UV irradiation due to its large band gap (3.2 eV), the BFO nanocrystals exhibit their obvious advantage making use of the visible-light due to their small band gaps. This is invaluable in increasing the photocatalytic reaction by using the visible sunlight.

4.2. BFO Nanoislands. Up to date, much work about the low-dimensional BFO nanostructures is mainly focused on the BFO nanoparticles (0D) and nanofilms (2D), and little work is reported on the BFO nanoislands. Geometrically, BFO nanoislands are a class of systems that bridge the gap between the BFO nanoparticles and BFO ultrathin films. Compared

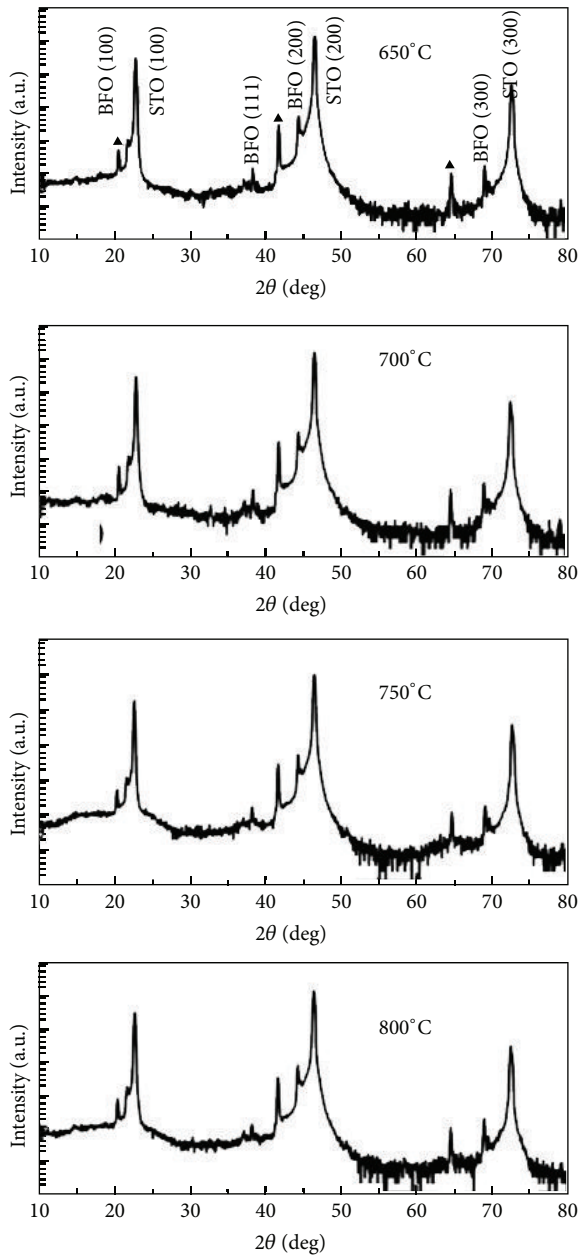

Figure 3: XRD patterns of the epitaxial $BiFeO_3$ nanoislands fabricated on $SrTiO_3$ (100) single crystal substrates by chemical assembled method, and postannealed at 650°C; 700°C; 750°C; and 800°C for 1 hour. The diffraction peaks labeled by ▲ were from the $SrTiO_3$ (100) single crystal substrates diffracted by the Cu-Kβ line due to the remaining Cu-Kβ radiation.

with BFO thin films, they have free-standing sidewalls that tend to suppress the formation of a nonuniform in-plane polarization due to the appearance of depolarizing field, similar to the ferromagnetic particles. On the other hand, relative to the (confined in all three dimensions) nanoparticles, the BFO nanoislands have large aspect ratio and likely to behave similarly to thin films when the polarization is out of plane. Therefore, it is expected that multiferroic BFO nanoislands should exhibit some kind of a "particle-to-thin film" crossover behavior and related novel effects depending on the aspect ratio and the type of bulk polarization ordering. Furthermore, due to the geometrical similarity between the multiferroic BFO nanoislands and microelectronic devices based on the multiferroic BFO nanomaterials, it is useful for simulating working conditions of real microelectronic devices [33, 34].

Recently, Hang et al. [29] reported the epitaxial growth of multiferroic BFO nanoislands on $SrTiO_3$ (100) and Nb-doped $SrTiO_3$ (100) single crystal substrates by chemical self-assembled method. By this method, they synthesized the epitaxial multiferroic BFO nanoislands *via* postannealing process in the temperature range of 650–800°C, and the lateral sizes of the BFO nanoislands were in the range of 50–160 nm and height of 6–12 nm. With increasing the postannealing temperature, the morphology of the BFO nanoislands in the (100) growth plane evolved from triangled to squared, and then to plated shapes. Ferroelectric characteristics of a single epitaxial BFO nanoisland (with lateral size of ~ 50 nm and height of 12 nm) grown on Nb-doped $SrTiO_3$ (100) single crystal substrate was characterized by PFM images. The results demonstrated that fractal ferroelectric domains existed in the single BFO nanoisland, and self-biased polarization was also observed within this multiferroic nanoisland. This phenomenon can be ascribed to the interfacial stress caused by the lattice misfit between the BFO nanoisland and the $SrTiO_3$ single crystal substrate.

By using the top-down approach such as FIB milling method, Morelli et al. [27] fabricated the arrays of epitaxial BFO islands with flat top surfaces and lateral sizes down to 250 nm by starting from a continuous BFO thin film. PFM images showed that the as-fabricated BFO nanoislands preserved ferroelectric properties with switchable polarization and exhibited retention of polarization state at least for several days. As compared with the parent thin film, the BFO nanoislands exhibit a certain degree of imprint behavior, as shown in Figure 9. That is due to the existence of the defects at the interface between the BFO film and $SrRuO_3$ substrate, and on the sidewalls of the islands.

4.3. BFO Nanowires, Nanotubes, and Their Arrays. In the last decade low-dimensional BFO nanostructures have received much attention because of their superior physical and chemical properties. Among them, BFO nanowires and nanotubes are especially attractive for nanoscience studies and nanotechnology applications, which are ascribed to that the BFO nanowires and/or nanotubes are not only used as the building blocks of future nanodevices, but also offer fundamental scientific opportunities for investigating the intrinsic size effects of physical properties.

Nowadays BFO nanowires, nanorods, nanotubes, and their arrays have been fabricated by the template-aided synthesis. However, all the products prepared by this method exhibit polycrystalline structures due to the heterogeneous nucleation on the pore walls; there are very few reports on the synthesis of single crystalline nanowires through this method. To better understand the intrinsic size effects of physical properties, high quality of one-dimensional single crystalline BFO nanowires is highly required. Recently,

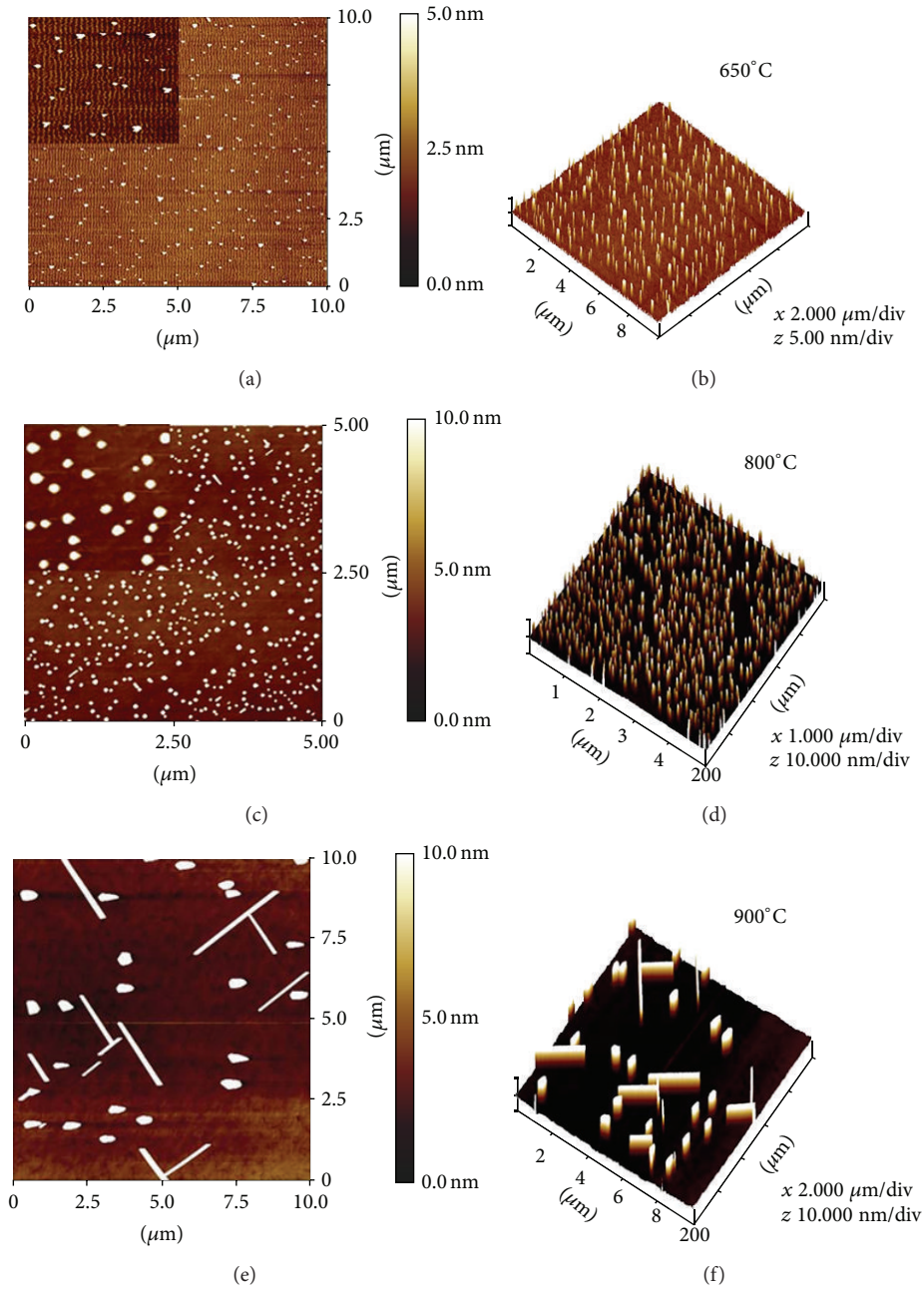

FIGURE 4: AFM images of the epitaxial $BiFeO_3$ nanoislands postannealed at ((a), (b)) 650°C, ((c), (d)): 800°C, ((e), (f)): 900°C for 1 h. The left AFM images are two-dimensional ones and the right ones are the corresponding 3-dimensional ones. The insets in (a) and (c) are the enlarged AFM images of the local surface areas.

Liu et al. [22] reported the synthesis of single-crystalline BFO nanowires (45–200 nm in diameter) by solvothermal method and measured their magnetic properties by superconducting quantum interference device (SQUID) at room temperature and low temperatures, as shown in Figure 10. Li et al. [35] also synthesized the BFO nanowires by solvothermal method (40–200 nm in diameter and several micrometers in length) and characterized a single BFO nanowire by PFM. The results shows the x and z-PFM hysteresis loops which clearly reveals the ferroelectric property of a single BFO nanowire.

The BFO nanowire (with diameter of 20 nm) arrays are also fabricated by template-assisted sol-gel technique [36]. Their ferroelectric and dielectric properties are demonstrated in Figure 11. Figure 11(a) shows the polarization of BFO nanowire arrays as a function of applied electric field about 600 kV/cm with a frequency (ν) = 10 kHz at room temperature. The observed P-E hysteresis loop exhibits well-saturated rectangular shape due to the presence of less oxygen-related defects and phase purity of the nanowires. The high value of saturation polarization was around 54 $\mu C/cm^2$ observed

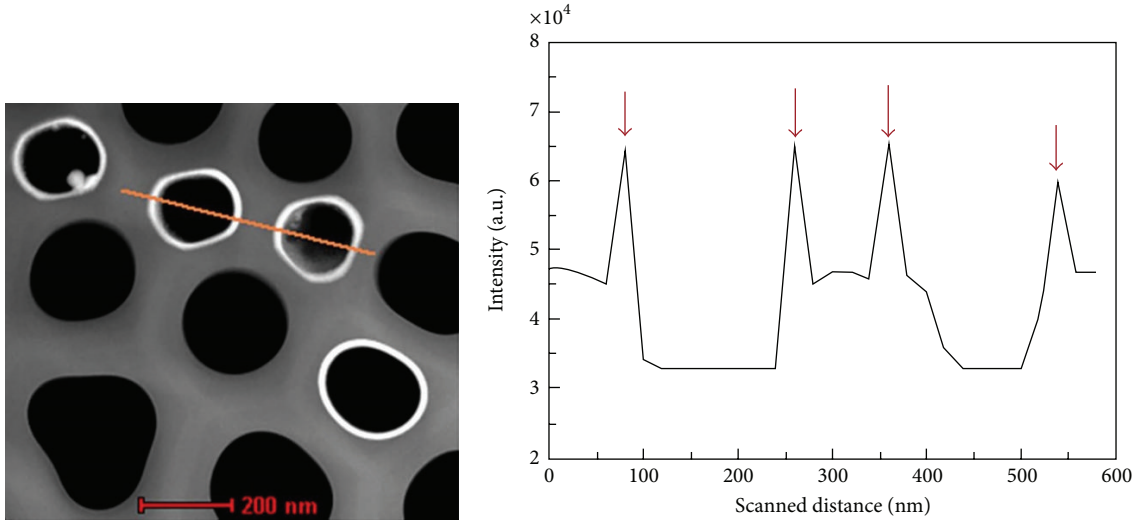

(a) (b)

Figure 5: (a) STEM image of the $BiFeO_3$ nanorings, (b) line scan of the intensity distribution of the STEM image contrast of the $BiFeO_3$ nanorings (the scanned line indicated in (a)).

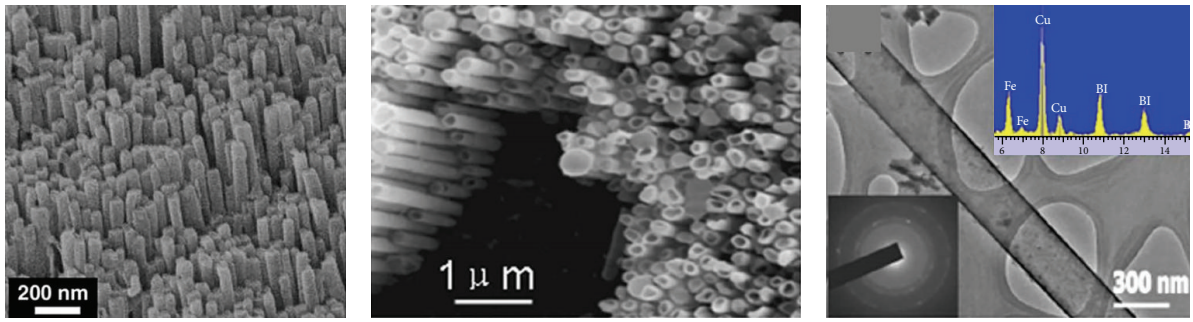

(a) (b) (c)

Figure 6: (a) SEM image of the $BiFeO_3$ nanowire array, (b) top-view of the nanochannel porous alumina filled with $BiFeO_3$ nanotubes, (c) TEM image of an isolated $BiFeO_3$ nanotube, the left inset shows the corresponding SAED pattern and the right inset shows the EDX spectrum.

at 535 kV/cm applied electric field. Figure 11(b) displays the relative dielectric constant (ε) of the BFO nanowire arrays as a function of frequency. A monotonous decrease of dielectric constant and dielectric loss was observed as Maxwell-Wagner type interfacial polarization, and in increasing the frequency, which was ascribed to good agreement with Koops phenomenological theory. The dielectric constant was measured to be as high as 492 at 1 KHz, which was due to space charge polarization resulting from the inhomogeneous dielectric structure. Recently, BFO nanotubes are also being prepared by a template synthesis involving the sol-gel technique [31]. Their ferroelectric and piezoelectric properties were characterized by PFM measurements. The piezoresponse d_{33} hysteresis loop of an individual BFO nanotube was measured using the conductive atomic force microscope tip applied with a 16.5 kHz ac electric field plus a swept dc voltage, and the result is shown in Figure 12(a). The decrease in d_{33} at high electric field, as shown in Figure 12(a), is ascribed to a consequence of the field-induced lattice hardening, which is typical for perovskite piezoelectrics. The significant piezoelectric characteristics illustrate the ferroelectric behavior of the BFO nanotubes. The dielectric constant and dielectric loss of the BFO nanotube arrays were also measured at room temperature as a function of the frequency in the range of 10^3–10^6 Hz, as shown in Figure 12(b). Both the dielectric constant and the dielectric loss show a remarkable decrease of up to 10^3 Hz and remain fairly constant afterward. The decrease in the dielectric constant with increasing the frequency represents the anomalous dispersion of the dielectric constant at low and intermediate frequencies, which has been explained by the phenomenon of dipole relaxation; while the variation in dielectric loss with frequency represents the relaxation absorption of the dielectrics.

5. Applications of BFO Nanostructures

BFO is one of several rare single-phase multiferroic materials that are both ferroelectric and weakly ferromagnetic at

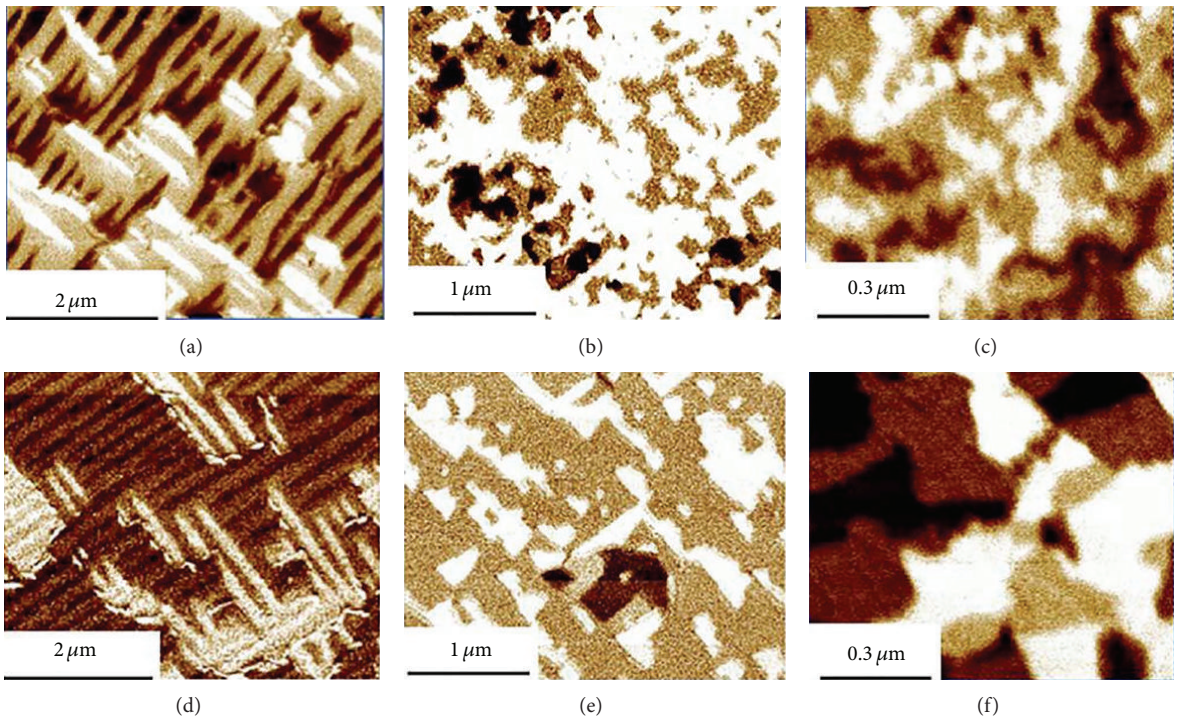

FIGURE 7: In-plane PFM images measured on (a) 120, (b) 15, and (c) 2 nm thick BFO samples on $SrTiO_3$ and in-plane PFM images measured on (d) 120, (e) 15, and (f) 2 nm thick BFO samples on $DySrO_3$ substrates.

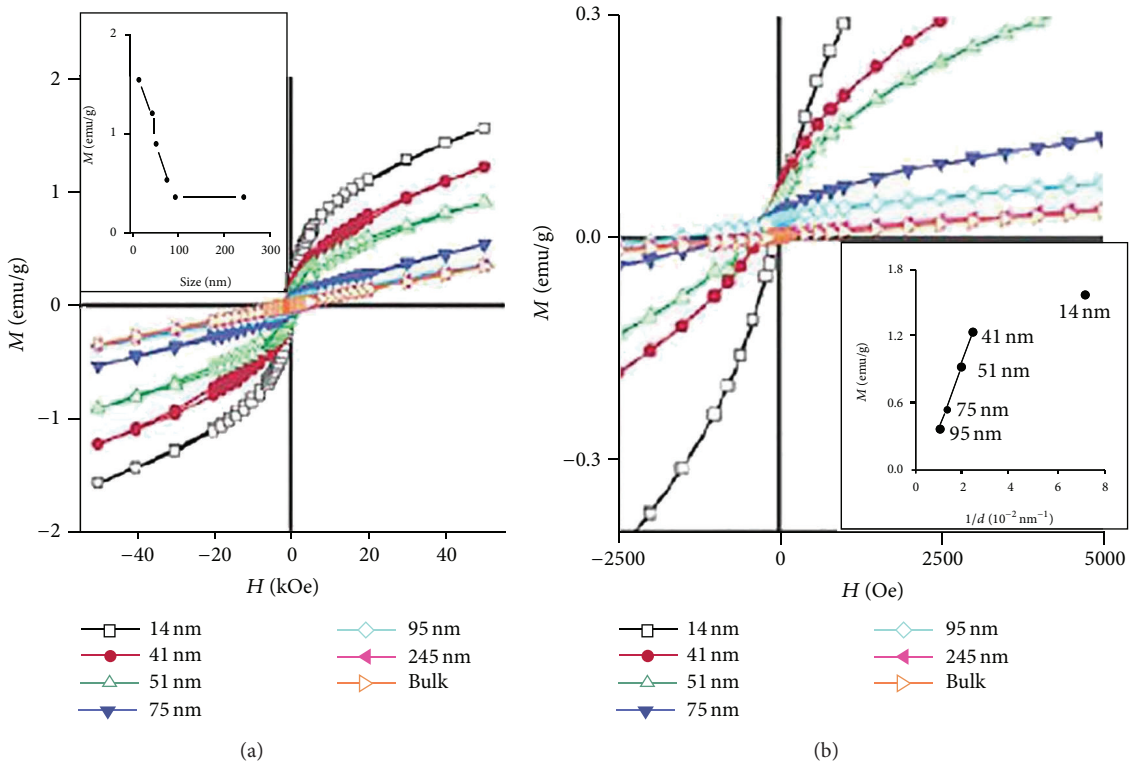

FIGURE 8: (a) Hysteresis loops measured at 300 K for $BiFeO_3$ nanoparticles with indicated sizes, (b) expanded plots of magnetization of $BiFeO_3$ nanoparticles with the return branches of the hysteresis loops omitted for clarity.

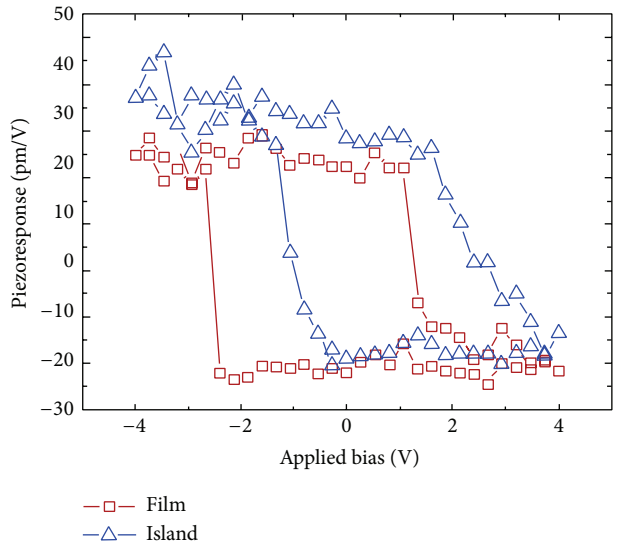

Figure 9: Local remanent piezoresponse hysteresis plots as resulting from measurements performed on an island (triangles) and on an area of the parent film (squares).

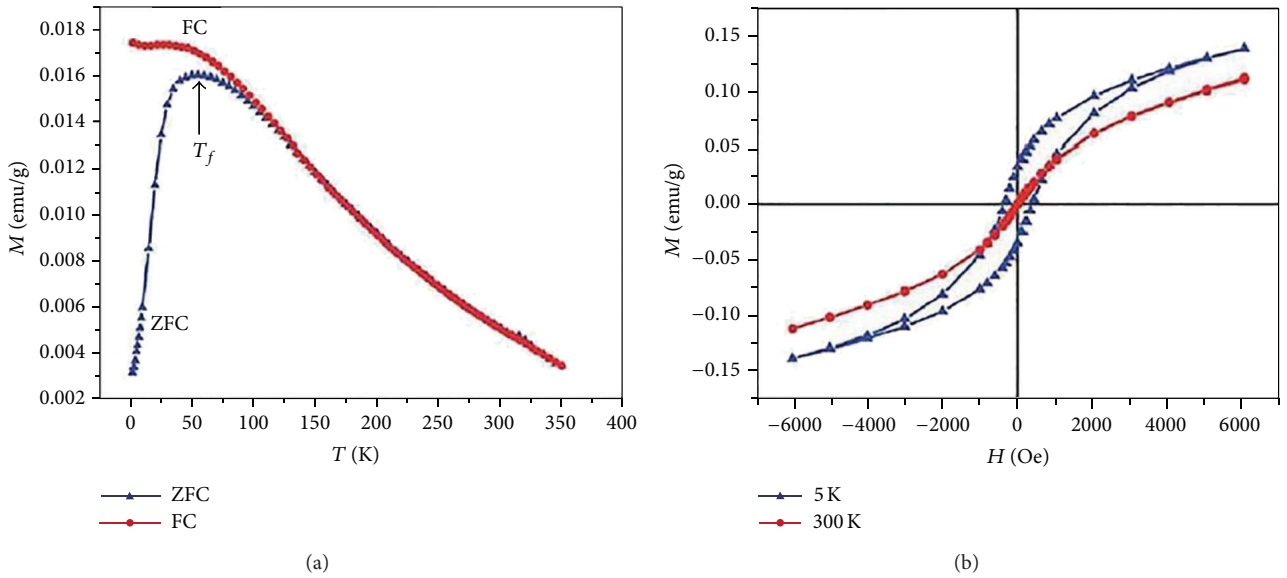

Figure 10: (a) Temperature dependence of zero-field-cooled (ZFC) and field-cooled (FC) susceptibility measured in a field of 100 Oe for $BiFeO_3$ nanowires, (b) *M-H* hysteresis loops for $BiFeO_3$ nanowires measured at 5 K and 300 K.

room temperature. Recent studies demonstrate that the BFO nanomaterials have spontaneous polarization enhancement, switchable ferroelectric diode effects, photovoltaic effects, piezoelectric, and THz radiation properties, which have potential applications in the fields of next-generation, lead-free, nondestructive memories, spin valve devices, actuators, and ultrahigh speed telecommunication devices [37].

BFO nanoparticles also exhibit good photocatalytic activities in visible-light region, which can be used as novel visible-light-responsive photocatalysts for degradation of organic compounds. For example, Zhu et al. [28] synthesized spherical perovskite-type single-crystalline BFO nanoparticles with diameters of 10–50 nm by microwave hydrothermal process, which exhibited efficient photocatalytic activity for the degradation of rhodamine B in aqueous solution under visible-light irradiation. Gao et al. [18] also synthesized BFO nanoparticles, which promoted the degradation rate of methyl orange to a high level under visible-light irradiation. In addition, Yu et al. [38] reported that perovskite-structured $BiFeO_3$ nanoparticles also exhibited excellent gas-sensing properties, which were potentially useful for high-quality gas sensors.

Due to the coupling of ferroelectric and antiferromagnetic vectors, reversing the ferroelectric polarization by an extern electric field also rotates the antiferromagnetic spins. Chu et al. [39] presented electric-field control of local

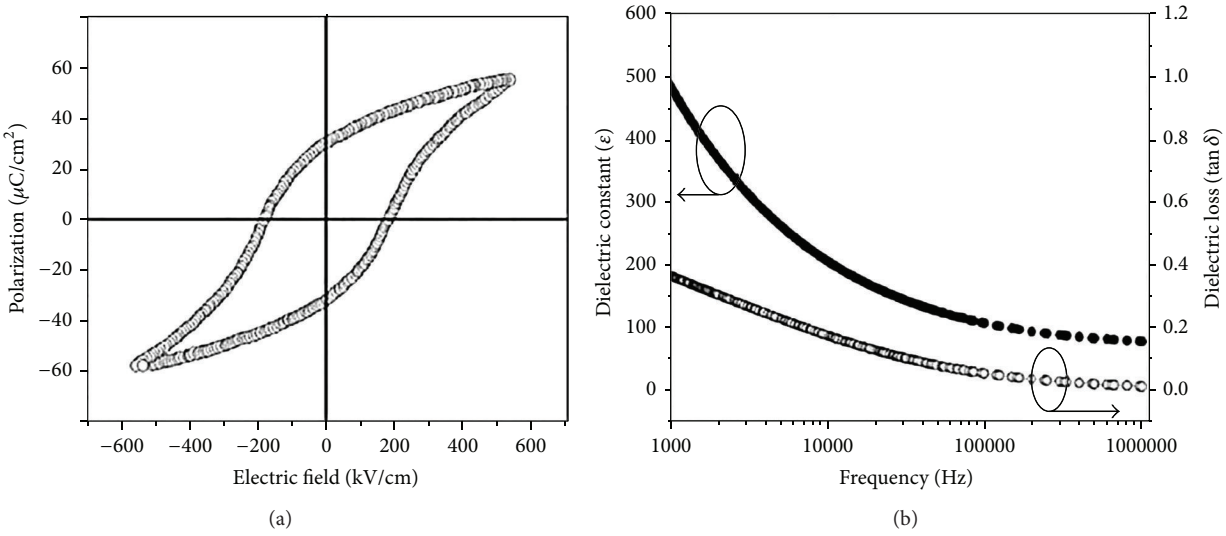

Figure 11: (a) Polarization versus applied electric field hysteresis loop, (b) relative dielectric constant and dielectric loss versus the frequency traits of $BiFeO_3$ nanowires.

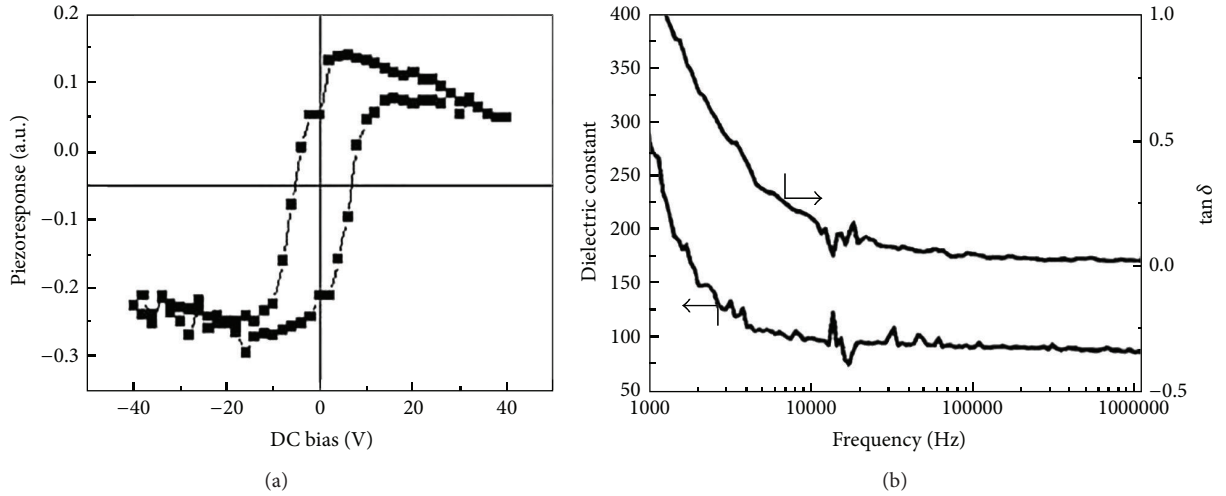

Figure 12: (a) Piezoelectric hysteresis loop of a single $BiFeO_3$ nanotube measured by PFM, (b) dielectric constant and dielectric loss measured at room temperature as a function of the frequency.

ferromagnetism through the coupling between the multiferroic BFO and a ferromagnet (CoFe in their work). They grew heterostructures of Au (2 nm)/CoFe (2.5–20 nm)/BFO (50–200 nm)/$SrRuO_3$ (25–50 nm) on $SrTiO_3$ (001)-oriented substrates. When applied an external in-plain electric field, they observed that the average magnetization direction in CoFe the ferromagnet rotates by 90°. The average magnetization direction changes back to the original state when applying the electric field again. If one suggests the original state as the binary signal "0," the rotated state of the magnetization direction is represented the signal "1." Therefore, the repeated such heterostructures can be used as essential building blocks to fabricate magnetoelectric random access memory elements.

Due to worldwide energy crisis, the investigation of materials for thin film photovoltaic cells is essential to renewable energy production. The large saturation polarization (~90 μC/cm^2) in BFO thin film and the band gap of BFO ($E_g \sim 2.67$ eV) smaller than many other ferroelectric perovskites make BFO the remarkable candidate for the photovoltaic cells. Yang et al. [40] reported photovoltaic devices based on BFO thin films and demonstrated the highest efficiency for the ferroelectric-based photovoltaic. They grew epitaxial ferroelectric BFO thin film by metal-organic chemical vapor deposition on (001)-oriented $SrTiO_3$ substrates with 50 nm epitaxial $SrRuO_3$ as bottom electrodes. Figure 13(a) shows a set of polarization-electric field hysteresis loops as a function of the test frequency which reveals a strong diode-like behavior, characterized by a large, directional leakage at negative voltages. Figure 13(b) shows the *I-V* curves taken both in dark and under 285 mW/cm^2 white-light illumination which reveals diode-like behavior and a photovoltaic effect of the heterostructure. External quantum efficiency (EQE)

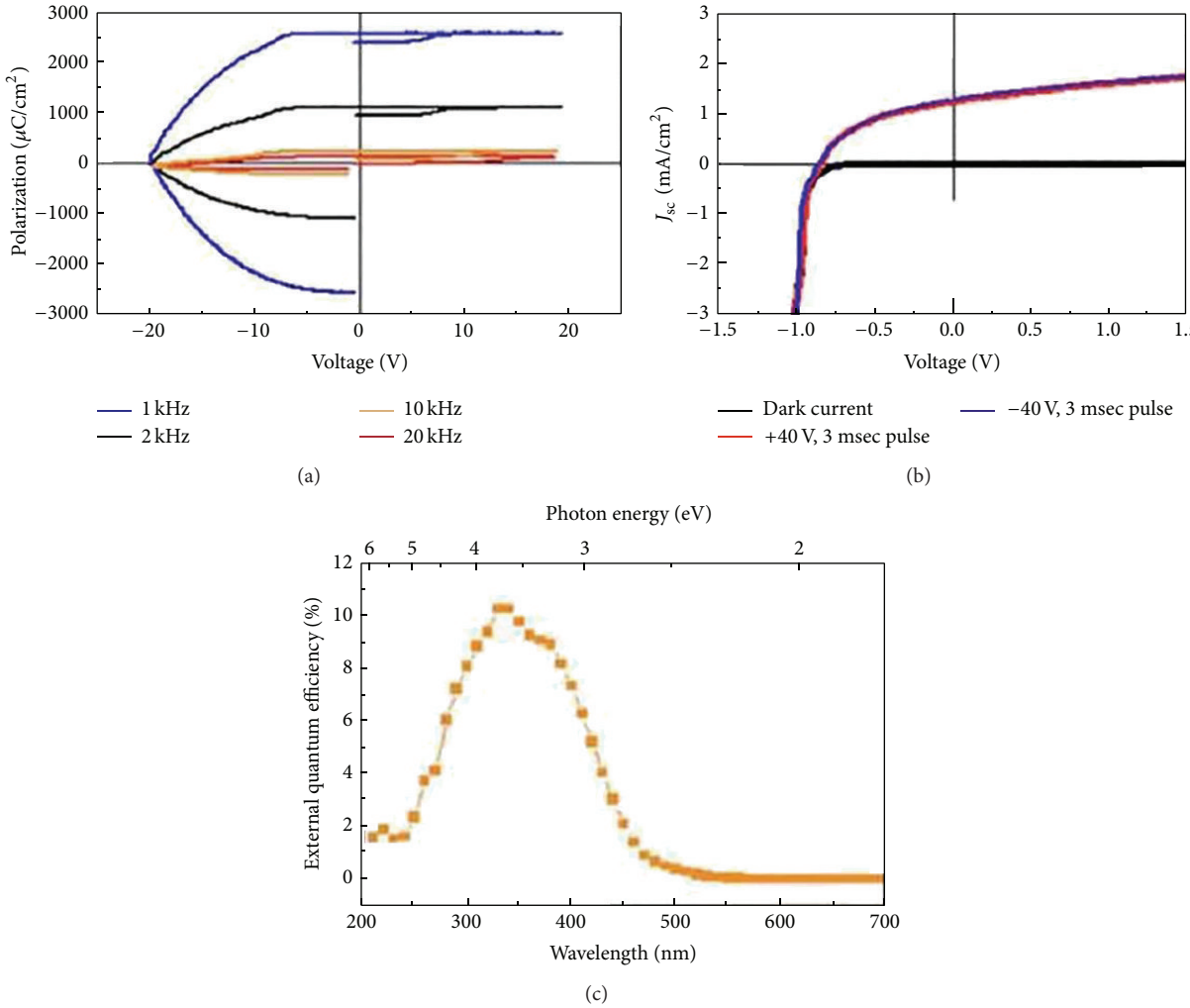

FIGURE 13: (a) Polarization-electric field hysteresis loops at various frequencies reveal diode-like behavior in one direction, (b) light (red and blue) and dark (black curve, running through the origin) *I-V* measurements completed at 2.85 suns intensity reveal photovoltaic effects in these device structures. There is no observed change in the light *I-V* response upon application of an electric field and (c) average EQE measurements for five different contacts on a single sample reveal efficiencies ~10% under illumination with band gap light.

measurement is showed in Figure 13(c) which reveals that the maximum conversion efficiency (~10%) is observed when the photon energy is larger than the band gap of BFO and drop-off at the shortest wavelength (<325 nm).

6. Conclusions

This paper reviews the recent research progress of low-dimensional BFO nanostructures, including their fabrication, property, structural characterization, and applications. Perovskite-type BFO as one of the few known single-phase multiferroics that possesses ferroelectricity and antiferromagnetism at room temperature. Its low-dimensional nanostructures are much attractive in the applications of multistate storage, magnetoelectric sensor, and spintronic devices. As the feature sizes of the microelectronic enter into nanoscale, there are still some problems that need to be solved in fabrication, characterization, and application of BFO low-dimensional nanostructures. For instance, in BFO nanostructures there exist quantum size effect, (ferroelectric and magnetoelectric) size effect, and surface/interface effect; all these effects must be considered together from experimental and theoretical researches, which are fundamental to developing the new generation of revolutionary electronic nanodevices. Although the BFO has good ferroelectricity, its weak ferromagnetism is highly required to be enhanced, which could be achieved in low-dimensional nanostructures. Therefore, deeper understanding of the fundamentals of the BFO low-dimensional nanostructures with the development of advanced technology and exploring the coexistrnce of ferroelectricity and ferromagnetism with strong coupling between them will be the future direction of BFO nanomaterials researches.

Conflict of Interests

The authors declare that there is no conflict of interests regarding the publication of this paper.

Acknowledgments

This work was partially supported by National Natural Science Foundation of China (Grant nos. 11174122 and 11134004), National Basic Research Program of China (Grant nos. 2009CB929503 and 2012CB619400), and the open project from National Laboratory of Solid State Microstructures, Nanjing University.

References

[1] H. Schmid, "Multi-ferroic magnetoelectrics," *Ferroelectrics*, vol. 162, no. 1, pp. 317–338, 1994.

[2] B. B. van Aken, J. R. Rivera, H. Schmid, and M. Fiebig, "Observation of ferrotoroidic domains," *Nature*, vol. 449, no. 7163, pp. 702–705, 2007.

[3] N. A. Spaldin and M. Fiebig, "The renaissance of magnetoelectric multiferroics," *Science*, vol. 309, no. 5733, pp. 391–392, 2005.

[4] C. Ederer and N. A. Spaldin, "Weak ferromagnetism and magnetoelectric coupling in bismuth ferrite," *Physical Review B: Condensed Matter and Materials Physics*, vol. 71, no. 6, Article ID 060401, 4 pages, 2005.

[5] C. Ederer and N. A. Spaldin, "Influence of strain and oxygen vacancies on the magnetoelectric properties of multiferroic bismuth ferrite," *Physical Review B*, vol. 71, no. 22, Article ID 224103, 9 pages, 2005.

[6] M. Kumar and K. L. Yadav, "Study of room temperature magnetoelectric coupling in Ti substituted bismuth ferrite system," *Journal of Applied Physics*, vol. 100, no. 7, Article ID 074111, 4 pages, 2006.

[7] D. H. Wang, W. C. Goh, M. Ning, and C. K. Ong, "Effect of Ba doping on magnetic, ferroelectric, and magnetoelectric properties in mutiferroic $BiFeO_3$ at room temperature," *Applied Physics Letters*, vol. 88, no. 21, Article ID 212907, 3 pages, 2006.

[8] T. Zhao, A. Scholl, F. Zavaliche et al., "Electrical control of antiferromagnetic domains in multiferroic $BiFeO_3$ films at room temperature," *Nature Materials*, vol. 5, no. 10, pp. 823–829, 2006.

[9] T. Park, G. C. Papaefthymiou, A. J. Viescas, A. R. Moodenbaugh, and S. S. Wong, "Size-dependent magnetic properties of single-crystalline multiferroic $BiFeO_3$ nanoparticles," *Nano Letters*, vol. 7, no. 3, pp. 766–772, 2007.

[10] H. Zhang and K. Kajiyoshi, "Hydrothermal synthesis and size-dependent properties of multiferroic bismuth ferrite crystallites," *Journal of the American Ceramic Society*, vol. 93, no. 11, pp. 3842–3849, 2010.

[11] R. R. Das, D. M. Kim, S. H. Baek et al., "Synthesis and ferroelectric properties of epitaxial $BiFeO_3$ thin films grown by sputtering," *Applied Physics Letters*, vol. 88, no. 24, Article ID 242904, 3 pages, 2006.

[12] R. Mazumder, P. S. Devi, D. Bhattacharya, P. Choudhury, A. Sen, and M. Raja, "Ferromagnetism in nanoscale $BiFeO_3$," *Applied Physics Letters*, vol. 91, no. 6, Article ID 062510, 3 pages, 2007.

[13] S. M. Stratulat, X. L. Lu, A. Morelli, D. Hesse, W. Erfurth, and M. Alexe, "Nucleation-induced self-assembly of multiferroic $BiFeO_3$- $CoFe_2O_4$ nanocomposites," *Nano Letters*, vol. 13, no. 8, pp. 3884–3889, 2013.

[14] R. Nath, S. Hong, J. A. Klug et al., "Effects of cantilever buckling on vector piezoresponse force microscopy imaging of ferroelectric domains in $BiFeO_3$ nanostructures," *Applied Physics Letters*, vol. 96, no. 16, Article ID 163101, 3 pages, 2010.

[15] M. Park, S. Hong, J. A. Klug et al., "Three-dimensional ferroelectric domain imaging of epitaxial $BiFeO_3$ thin films using angle-resolved piezoresponse force microscopy," *Applied Physics Letters*, vol. 97, no. 11, Article ID 112907, 3 pages, 2010.

[16] R. Nath, S. Hong, J. A. Klug et al., "Effects of cantilever buckling on vector piezoresponse force microscopy imaging of ferroelectric domains in $BiFeO_3$ nanostructures," *Applied Physics Letters*, vol. 96, Article ID 163101, 2010.

[17] J. K. Kim, S. S. Kim, and W. J. Kim, "Sol-gel synthesis and properties of multiferroic $BiFeO_3$," *Materials Letters*, vol. 59, no. 29-30, pp. 4006–4009, 2005.

[18] F. Gao, X. Chen, K. Yin et al., "Visible-light photocatalytic properties of weak magnetic $BiFeO_3$ nanoparticles," *Advanced Materials*, vol. 19, no. 19, pp. 2889–2892, 2007.

[19] X.-Z. Chen, Z.-C. Qiu, J.-P. Zhou, G. Zhu, X.-B. Bian, and P. Liu, "Large-scale growth and shape evolution of bismuth ferrite particles with a hydrothermal method," *Materials Chemistry and Physics*, vol. 126, no. 3, pp. 560–567, 2011.

[20] S. H. Han, K. S. Kim, H. G. Kim et al., "Synthesis and characterization of multiferroic $BiFeO_3$ powders fabricated by hydrothermal method," *Ceramics International*, vol. 36, no. 4, pp. 1365–1372, 2010.

[21] Y. Wang, G. Xu, Z. Ren et al., "Mineralizer-assisted hydrothermal synthesis and characterization of $BiFeO_3$ nanoparticles," *Journal of the American Ceramic Society*, vol. 90, no. 8, pp. 2615–2617, 2007.

[22] B. Liu, B. Hu, and Z. Du, "Hydrothermal synthesis and magnetic properties of single-crystalline $BiFeO_3$ nanowires," *Chemical Communications*, vol. 47, no. 28, pp. 8166–8168, 2011.

[23] L. Zhang, X. Cao, Y. Ma, X. Chen, and Z. Xue, "Polymer-directed synthesis and magnetic property of nanoparticles-assembled $BiFeO_3$ microrods," *Journal of Solid State Chemistry*, vol. 183, no. 8, pp. 1761–1766, 2010.

[24] T. J. Park, Y. Mao, and S. S. Wong, "Synthesis and characterization of multiferroic $BiFeO_3$ nanotubes," *Chemical Communications*, no. 23, pp. 2708–2709, 2004.

[25] X. Y. Zhang, J. Y. Dai, and C. W. Lai, "Synthesis and characterization of highly ordered $BiFeO_3$ multiferroic nanowire arrays," *Progress in Solid State Chemistry*, vol. 33, no. 2–4, pp. 147–151, 2005.

[26] F. Gao, Y. Yuan, K. F. Wang et al., "Preparation and photoabsorption characterization $BiFeO_3$ nanowires," *Applied Physics Letters*, vol. 89, no. 10, Article ID 102506, 3 pages, 2006.

[27] A. Morelli, F. Johann, N. Schammelt, D. McGrouther, and I. Vrejoiu, "Mask assisted fabrication of nanoislands of $BiFeO_3$ by ion beam milling," *Journal of Applied Physics*, vol. 113, no. 15, Article ID 154101, 4 pages, 2013.

[28] X. H. Zhu, Q. M. Hang, Z. B. Xing et al., "Microwave hydrothermal synthesis, structural characterization, and visible-light photocatalytic activities of single-crystalline bismuth ferric nanocrystals," *Journal of the American Ceramic Society*, vol. 94, no. 8, pp. 2688–2693, 2011.

[29] Q. M. Hang, X. H. Zhu, Z. J. Tang, Y. Song, and Z. G. Liu, "Self-assembled perovskite epitaxial multiferroic $BiFeO_3$ nanoislands," *Advanced Materials Research*, vol. 197-198, pp. 1325–1331, 2011.

[30] J. Zhou, S. Liang, S. Y. Li, Z. D. Liu, Y. Y. Zhu, and X. H. Zhu, "Advances in low-dimensional $BiFeO_3$ multiferroic nanostructures," *Journal of Chinese Electron Microscopy Society*, vol. 32, no. 6, pp. 504–524, 2013.

[31] X. Y. Zhang, C. W. Lai, X. Zhao, D. Y. Wang, and J. Y. Dai, "Synthesis and ferroelectric properties of multiferroic $BiFeO_3$ nanotube arrays," *Applied Physics Letters*, vol. 87, no. 14, Article ID 143102, 3 pages, 2005.

[32] Y. H. Chu, T. Zhao, M. P. Cruz et al., "Ferroelectric size effects in multiferroic $BiFeO_3$ thin films," *Applied Physics Letters*, vol. 90, no. 25, Article ID 252906, 3 pages, 2007.

[33] I. Naumov and A. M. Bratkovsky, "Unusual polarization patterns in flat epitaxial ferroelectric nanoparticles," *Physical Review Letters*, vol. 101, no. 10, Article ID 107601, 4 pages, 2008.

[34] S. K. Streiffer and D. D. Fong, "Phase transitions in nanoscale ferroelectric structures," *MRS Bulletin*, vol. 34, no. 11, pp. 832–837, 2009.

[35] S. Li, R. Nechache, C. Harnagea, L. Nikolova, and F. Rosei, "Single-crystalline $BiFeO_3$ nanowires and their ferroelectric behavior," *Applied Physics Letters*, vol. 101, no. 19, Article ID 192903, 3 pages, 2012.

[36] G. S. Lotey and N. K. Verma, "Magnetoelectric coupling in multiferroic $BiFeO_3$ nanowires," *Chemical Physics Letters*, vol. 579, no. 30, pp. 78–84, 2013.

[37] M. Bibes and A. Barthélémy, "Multiferroics: towards a magnetoelectric memory," *Nature Materials*, vol. 7, no. 6, pp. 425–426, 2008.

[38] X. L. Yu, Y. Wang, Y. M. Hu, C. Cao, and H. L. Chan, "Gas-sensing properties of perovskite $BiFeO_3$ nanoparticles," *Journal of the American Ceramic Society*, vol. 92, no. 12, pp. 3105–3107, 2009.

[39] Y. H. Chu, L. W. Martin, M. B. Holcomb et al., "Electric-field control of local ferromagnetism using a magnetoelectric multiferroic," *Nature Materials*, vol. 7, no. 6, pp. 478–482, 2008.

[40] S. Y. Yang, L. W. Martin, S. J. Byrnes et al., "Photovoltaic effects in $BiFeO_3$," *Applied Physics Letters*, vol. 95, no. 6, Article ID 062909, 3 pages, 2009.